

1 **Regional flow conditions associated with stratocumulus cloud-eroding**  
2 **boundaries over the southeast Atlantic**

3 Laura M. Tomkins<sup>\*†</sup>, David B. Mechem

4 *Department of Geography and Atmospheric Science, University of Kansas, Lawrence, KS.*

5 Sandra E. Yuter, Spencer R. Rhodes

6 *Department of Marine, Earth, and Atmospheric Sciences, North Carolina State University,*

7 *Raleigh, NC*

8 <sup>\*</sup>*Corresponding author:* Laura M. Tomkins, lmtomkin@ncsu.edu

9 <sup>†</sup>*Current affiliation:* Center for Geospatial Analytics, North Carolina State University, Raleigh, NC

## ABSTRACT

10 Large, abrupt clearing events have been documented in the marine stratocumulus cloud deck over  
11 the subtropical Southeast Atlantic Ocean. In these events, clouds are rapidly eroded along a line  
12 hundreds–to–thousands of kilometers in length that generally moves westward away from the coast.  
13 Because marine stratocumulus clouds exert a strong cooling effect on the planet, any phenomenon  
14 that acts to erode large areas of low clouds may be climatically important. Previous satellite-based  
15 research suggests that the cloud-eroding boundaries may be caused by westward-propagating  
16 atmospheric gravity waves rather than simple advection of the cloud. The behavior of the coastal  
17 offshore flow, which is proposed as a fundamental physical mechanism associated with the clearing  
18 events, is explored using the Weather Research and Forecasting model. Results are presented  
19 from several week-long simulations in the month of May when cloud-eroding boundaries exhibit  
20 maximum frequency. Two simulations cover periods containing multiple cloud-eroding boundaries  
21 (active periods), and two other simulations cover periods without any cloud-eroding boundaries  
22 (null periods). Passive tracers and an analysis of mass flux are used to assess the character of  
23 the diurnal west-African coastal circulation. Results indicate that the active periods containing  
24 cloud-eroding boundaries regularly experience stronger and deeper nocturnal offshore flow from  
25 the continent above the marine boundary layer, compared to the null periods. Additionally, we find  
26 that the boundary layer height is higher in the null periods than in the active periods, suggesting  
27 that the active periods are associated with areas of thinner clouds that may be more susceptible to  
28 cloud erosion.

## 29 **1. Introduction**

30 Stratocumulus clouds are an important component of the climate system. Stratocumulus cover  
31 vast areas of the planet and are more abundant than any other type of cloud (Wood 2012). In  
32 addition to their large areal coverage, they scatter back to space a large portion of incoming solar  
33 radiation, and because the cloud-top temperature is only slightly cooler than the underlying surface,  
34 they emit nearly the same amount of infrared radiation as the surface, thus exerting a strong cooling  
35 effect on the planet (Hartmann et al. 1992). Large changes to stratocumulus area coverage or  
36 optical properties will therefore substantially impact the regional radiation budget. Unfortunately,  
37 representing stratocumulus in general circulation models (GCMs) remains an ongoing challenge  
38 (Bony and Dufresne 2005; Lin et al. 2014; Wyant et al. 2015).

39 Dramatic cloud-eroding boundaries have been documented in marine stratocumulus clouds over  
40 the southeast Atlantic (SEA) ocean off the western coast of Africa (Yuter et al. 2018). These  
41 clearing events arise as long lines ( $>1000$  km) of sharp cloudiness transitions that cross the coast  
42 around local midnight and usually propagate westward at a speed of  $\sim 10$  m s<sup>-1</sup>. Large areas of the  
43 stratocumulus cloud field rapidly erode along these sharp boundaries (time scale  $<15$  min), leaving  
44 behind either clear skies or significantly thinner clouds, which allows increased solar radiation to  
45 reach the surface. Since the cloud clearing occurs overnight as well as during the day, no shortwave  
46 feedbacks are required. Below the boundary layer inversion, southerly flow associated with the  
47 climatologically dominant subtropical high pressure is typically observed over this region during  
48 these events. Sequences of satellite images show the cloud-eroding boundaries moving westward  
49 while the clouds themselves move northward. This indicates that this cloud-eroding phenomenon  
50 is not driven by the southerly flow that exists within the boundary layer and at cloud level.

51 Yuter et al. (2018) hypothesize that, instead of advection, gravity waves are a likely mechanism  
52 for rapidly eroding large areas of cloud over the SEA. Gravity waves have been demonstrated  
53 to strongly influence cloud properties over the southeast Pacific (SEP) ocean (O'Dell et al. 2008;  
54 Garreaud and Muñoz 2004; Rahn and Garreaud 2010). The gravity waves over the SEA are thought  
55 to be excited by an interaction between the offshore flow from the high terrain of coastal Africa  
56 and the stratocumulus-topped boundary layer. A hypothetical gravity wave moving through the  
57 cloud field would influence cloud properties as follows. For a well-mixed boundary layer, upward  
58 wave motion increases the boundary layer depth, thickening the cloud by a proportional amount  
59 and increasing the liquid water path (LWP; note that LWP scales as the square of the cloud depth,  
60 i.e.,  $LWP \sim h^2$ ). Downward wave motion, on the other hand, reduces the boundary layer depth,  
61 resulting in a thinner cloud. Ordinarily, after the wave passes through, the cloud would return to  
62 its initial state. In the cloud-eroding cases, however, the cloud is partially or completely cleared.  
63 This cloud-eroding phenomenon, therefore, necessitates an irreversible aspect to the gravity-wave  
64 mechanism. The speed of the cloud-clearing process and that fact that this type of cloud-clearing  
65 often occurs overnight suggests that previous explanations for irreversible cloud transformations  
66 based on precipitation or radiative feedbacks (Allen et al. 2013; Connolly et al. 2013) are not  
67 primary mechanisms. Synoptic and microphysical influences on cloud clearing (e.g., Kloesel  
68 1992; Crosbie et al. 2016) also act too slowly to explain cloud-clearing occurring in a few 10's of  
69 minutes.

70 Enhanced entrainment is proposed as the particular irreversibility mechanism, whereby gravity-  
71 wave passage promotes stronger entrainment, leading to warming and drying within the cloud level  
72 at the top of the boundary layer (Yuter et al. 2018). Satellite observations of the cloud boundaries  
73 often show high-frequency wave features at the edge of the cloud boundaries, also suggesting that  
74 gravity waves may be a factor in the cloud-eroding boundaries. Although the cloud field may not

75 completely clear, we refer to these transformations as irreversible because over a short period the  
76 cloud remains eroded. After clearing, cloud usually reforms after several hours or at most a day  
77 later. Rapid cloud clearing may also be aided by the on average thinner clouds over the SEA as  
78 compared to the SEP (Zuidema et al. 2016).

79 The geography of the subtropical western coast of Africa yields a superposition of ups-  
80 lope/downslope flows and sea/land breezes. The coasts of Angola and Namibia feature an es-  
81 carpment that forms the western edge of a broad region of inland plateau. When the land heats up  
82 during the day, a sea breeze is established and onshore and upslope flow prevails. The opposite is  
83 true overnight when the land cools down and a land breeze and downslope flow develops. Assum-  
84 ing the cloud-eroding boundaries are related to the strength of the offshore flow, work from Qian  
85 et al. (2012) suggests that increasing terrain height may strengthen the overnight offshore flow and  
86 and increase the potential for gravity waves.

87 A key characteristic of the cloud-eroding boundaries is that they originate adjacent to the coast  
88 near local midnight. Our proposed mechanism for explaining the cloud-eroding boundaries over the  
89 SEA involves three distinct components: 1) the nocturnal offshore flow (land breeze and downslope  
90 flow) from the continent; 2) the interaction of this offshore flow with the marine boundary layer via  
91 the excitation of gravity waves; and 3) a mechanism that renders the cloud field irreversibly modified  
92 (cleared) after gravity-wave passage. We use the Weather Research and Forecasting (WRF) model  
93 to address aspects of the first two components above by characterizing and comparing the behavior  
94 of the coastal circulation for multiple 7-day periods during the month of May that experience  
95 cloud-clearing events to periods that do not. The simulation methodology and experimental design  
96 are described in Section 2. Section 3 discusses the results of the simulations. Section 4 will  
97 consider the implications of the results, and Section 5 will present the conclusions of the study.

## 98 **2. Methods**

99 The proposed cloud-eroding hypothesis from Yuter et al. (2018) requires three separate mech-  
100 anisms: offshore flow, excitation of gravity waves, and a quasi-irreversible clearing mechanism.  
101 This research focuses on examining and characterizing the first mechanism, the offshore flow.

### 102 *a. Model Description*

103 All simulations use the Advanced Research WRF (ARW) model (version 3.9.1), which is based  
104 on three-dimensional, nonhydrostatic, compressible dynamics (Skamarock et al. 2008). The  
105 Mellor–Yamada–Janjic (MYJ) boundary layer parameterization is employed to represent subgrid-  
106 scale vertical transports (Janjic 1994). Horizontal diffusion is parameterized using Smagorinsky  
107 first-order closure (Smagorinsky 1963). Microphysical processes are parameterized using the  
108 Morrison 2-moment scheme (Morrison et al. 2009). The Kain–Fritsch (KF) scheme is used  
109 for the convective parameterization (Kain 2004). It should be noted that deep convection is  
110 scarce over our domain during this time of year, except for that associated with the Inter–Tropical  
111 Convergence Zone (ITCZ). All simulations employ the NOAH land surface model (Tewari et al.  
112 2004). Longwave radiation is parameterized with the Rapid Radiative Transfer Model (RRTM)  
113 scheme, and shortwave radiation is parameterized with the Dudhia scheme (Dudhia 1989; Mlawer  
114 et al. 1997). We ran a number of additional simulations with different boundary layer and convective  
115 parameterizations to test the sensitivity of the model to parameterization choice. For the boundary  
116 layer parameterization, we tested the Yonsei University scheme and the Mellor–Yamada Nakanishi  
117 Niino (MYNN) Level–2.5 scheme scheme (Hong et al. 2006; Nakanishi and Niino 2006). For  
118 the convective parameterization, we tested the Betts–Miller–Janjic (BMJ) scheme (Janjic 1994).  
119 Simulation results were not particularly sensitive to the choice of boundary layer and/or convective  
120 parameterizations.

121 The domain for the simulations extends from 12°W to 25°E in the east-west direction and 0°N  
122 to 28°S in the north-south direction (Fig. 1). Horizontal grid spacing is 10 km with 430 points  
123 in the east-west direction and 298 in the north-south direction (4300 km x 2980 km), with a time  
124 step of 40 seconds (Fig. 1). The domain is configured to include a substantial portion of the  
125 continent, especially the plateau region, to better resolve the diurnal heating and cooling processes  
126 responsible for the land/sea breeze circulation. Because the cloud-eroding boundaries often move  
127 as far west as 4°W, the domain also extends well out over the ocean. Initial simulations included a  
128 fine (3.33 km), nested domain within the coarse domain; however, the coarse mesh was sufficient  
129 in capturing the salient mesoscale features of the coastal circulation. Examining the clouds and  
130 entrainment behavior in detail (which we do not do in this project) will require simulations with  
131 a finer mesh. The vertical grid has 82 points with variable grid spacing to adequately resolve the  
132 boundary layer and inversion structure (Fig. 2b). In the lower 5 km, the grid spacing ranges from  
133 20 m to 400 m, and above that increases up to a maximum of 1000 m (Fig. 2a). The grid spacing  
134 near the inversion height is ~100 m similar to the regional modeling study of Nelson et al. (2016).

135 European Centre for Medium-Range Forecasts (ECMWF) interim reanalysis (ERA–Interim;  
136 Dee et al. (2011)) data, available every 6 hours (four times daily) with a 0.75°latitude/longitude  
137 grid spacing, provides initial and boundary conditions for the WRF simulations. Data assimilation  
138 update cycles are not employed throughout the simulation, so the ERA–Interim reanalysis influences  
139 the WRF simulations only by serving as the initial conditions and via the boundary forcing. Sea  
140 Surface Temperature (SST) data are provided from ERA–Interim reanalysis. Following Nelson  
141 et al. (2016), we consider the first 24 hours to be the spin-up period. Due to the coarse resolution  
142 of the ERA–Interim data, the initial conditions are very smooth. Over the first day, smaller-scale  
143 variability consistent with the WRF grid resolution develop, and by ~24 hours the finer-scale

144 variability in WRF has had a full chance to develop. We consider the model spin-up period to be  
145 complete when, visually, fine-scale structures have sufficiently developed.

146 For this analysis, boundary layer heights were calculated by finding gradients in vertical profiles  
147 of potential temperature. The lowest height between 200 m and 5000 m that has a potential  
148 temperature gradient exceeding 1.5 K / 100 m designates the boundary layer height. We note  
149 that regional models and GCMs consistently underestimate boundary layer heights (Wyant et al.  
150 2015; Nelson et al. 2016), so while we do not necessarily trust the absolute boundary layer heights  
151 presented in this analysis we do have confidence in the relative boundary layer heights.

#### 152 *b. Project Design and Case Selection*

153 Instead of concentrating on specific clearing events, we performed a series of 7-day simulation  
154 periods. All simulation periods take place during May coinciding with the highest frequency  
155 of clearing events (Yuter et al. 2018). Future work will simulate events in other months. Of  
156 the four, 7-day simulations, two were “active” periods during which most of the days included  
157 cloud-eroding boundaries, and two were “null” periods without clearing events. The periods were  
158 classified as active or null based on Yuter et al. (2018), who characterized 1911 days over five years  
159 as either having cloud-eroding boundaries present (“yes”), not having boundaries present (“no”),  
160 or possibly having boundaries present (“maybe”). Events were characterized using Moderate  
161 Resolution Imaging Spectroradiometer (MODIS) corrected reflectance data from the Aqua and  
162 Terra satellites (see methods of Yuter et al. (2018) for full details). We chose two periods of  
163 both active and null simulations to provide context and increase confidence in the results of each  
164 simulation. Table 1 shows the dates spanned by each simulation and whether each day had a  
165 clearing event (YES) or not (NO).

166 *c. Reanalysis Temperature Comparison*

167 Accurately representing the nocturnal offshore coastal flow thought to be a critical component of  
168 the cloud-clearing events requires that WRF capture the diurnal cycle of the 2-m air temperature.  
169 Our region of study has very few in situ observations with which we could validate our model, but  
170 as an effort to provide some confidence in our simulations, we compared 2-m temperatures among  
171 ERA–Interim (providing the initial and boundary conditions for our simulations), ERA5 (ECMWF  
172 Reanalysis 5th Generation; Hersbach and Dee (2016)), and MERRA2 (Modern-Era Retrospective  
173 analysis for Research and Applications, Version 2; Gelaro et al. (2017)) with the diurnal cycle  
174 from WRF to observe any potential discrepancies in the overnight minimum temperature. In  
175 particular, we are interested in differences in overnight minimum temperature among the reanalyses  
176 datasets and potential differences between the WRF model and its parent ERA–Interim reanalysis.  
177 Broad agreement among these would lend confidence that the WRF simulations are likely to be  
178 representing the offshore flow with sufficient fidelity. The diurnal cycle for each dataset is averaged  
179 over the red box in Figure 1 and results are presented in Figure 3. The diurnal cycle is similar  
180 for all four datasets, yet we note some minor discrepancies. In general, the reanalyses (red, blue,  
181 and green lines in Fig. 3) have higher afternoon maximums compared to the WRF simulations.  
182 For the morning minimum temperatures, there is more spread between each dataset. The average  
183 minimum temperature for WRF is 287.6 K, 288.9 K for ERA–Interim, 287.6 K for ERA5, and  
184 285.7 K for MERRA2. The WRF minimum temperature is only 1.3 K cooler than the ERA–Interim  
185 reanalysis used as the input. The ERA5 is slightly cooler than ERA–Interim, and MERRA2 is a  
186 few degrees cooler. In addition to the WRF simulations, both the ERA5 and MERRA2 datasets  
187 are output more frequently than the 6-hourly ERA–Interim and may be able to better represent  
188 the minimum temperature. This may explain why these datasets have a colder average minimum

189 temperature compared to the ERA–Interim. Regardless, these differences in temperature are not  
190 likely to influence our results and provide confidence that the WRF simulations produce similar  
191 temperatures compared to other available datasets.

### 192 **3. Results**

#### 193 *a. Synoptic overview*

194 The domain of our simulations lies largely in the subtropics, extending into the tropics and  
195 midlatitudes in the northern and southern part of the domain, respectively (Fig. 1). Maps of sea  
196 level pressure (SLP) during a representative time in the middle of each simulation at 0000 UTC are  
197 shown in Figure 4. Note that the local time over the western portion of the WRF domain is the same  
198 as UTC, whereas east of  $7.5^{\circ}\text{E}$ , the local time is UTC+0100. In this study, we consider UTC to be  
199 at or near the local time. As is discussed in the sections above, the surface is largely dominated  
200 by a semi-permanent high pressure over the ocean due to the descending branch of the Hadley cell  
201 circulation and the cool ocean. Additionally, during the austral autumn, high pressure also exists  
202 over the land and is often accompanied by a trough of low pressure along the coast, evident in  
203 all four simulations (Fig. 4). Although the mean SLP differs slightly across the four simulations,  
204 the SLP pattern differences are minor, suggesting that the clearing events are not tied to specific  
205 synoptic-scale features or patterns, a finding which is consistent with the results of (Yuter et al.  
206 2018). Additionally, middle- and upper-level fields indicated minimal minimal differences across  
207 the four simulations (not shown).

208 *b. Offshore flow*

209 1) PASSIVE TRACER FIELDS

210 In order to explore the behavior of the coastal circulation, we evaluate the evolution of a passive  
211 tracer over the simulation domain using the method of Blaylock et al. (2017). A nondimensional  
212 scalar tracer field is initialized with a value of unity over a defined volume at the beginning of  
213 the simulation. The tracer field is held fixed over that volume for the duration of the simulation,  
214 providing a source of the tracer which is then advected away from the region. Two tracer regions  
215 are used, one over land and one over the ocean. One tracer region is placed over land near the coast  
216 ( $12^{\circ}\text{E}$  to  $15^{\circ}\text{E}$ ,  $15^{\circ}\text{S}$  to  $17^{\circ}\text{S}$ ) where the elevation varies between 200 m and 1500 m to visualize the  
217 flow patterns associated with the land-sea breeze circulation. Another tracer region is initialized  
218 over the ocean ( $9^{\circ}\text{E}$  to  $11^{\circ}\text{E}$ ,  $15^{\circ}\text{S}$  to  $17^{\circ}\text{S}$ ) to observe the flow patterns within the boundary layer.  
219 The tracer field is initialized in the first six vertical levels of the model, up to around 160 m above  
220 the surface, covering an area of 22 x 23 grid points (220 km x 230 km). Figure 5 shows plan  
221 views and cross sections of the passive tracer fields originating over land at the middle (after first  
222 96 hours) and end (at the last hour) of the first active period. The plan views (Figs. 5a,b) show a  
223 quasi-integrated quantity of the tracer field which is calculated by adding up the value of the tracer  
224 field in each column. Note that over the source region the vertically summed tracer values can  
225 be greater than the initial value of this quantity, as the tracer is transported vertically and is then  
226 replenished in the source region. Animations of both tracer fields for four simulations presented  
227 here can be accessed in the supplemental material.

228 Supplemental animations S1 and S5 show movies of the tracer fields every hour during the first  
229 active period. Early in the simulation, the tracer field remains mostly over the continent (Fig. 5a,  
230 supplemental animation S1) but as the simulation progresses, the tracer field is evident further

231 out over the ocean (Fig. 5b, supplemental animation S1), eventually reaching as far out as 0°E.  
232 Similarly, the tracer field initialized over land in the second active period is advected far out over  
233 the ocean over the course of the simulation (Fig. 6b, supplemental animation S2). Vertical cross  
234 sections (through 15.5°S, black line in Fig. 5a,b) show the tracer field being lofted up to 3–4 km  
235 (~1.5–2.5 km AGL) over the land during the day when the diurnal heating causes upward motion  
236 (Figs. 5a,b, 6a,b, supplemental animations S1, S2). Additionally, the cross sections during the  
237 active periods show the tracer field being advected westward above the boundary layer during the  
238 overnight hours (Fig. 5d, 6d, supplemental animation S1, S2).

239 The tracer field initialized over land in the two null periods remains mostly over the continent  
240 and is not transported out over the ocean nearly as far as during the active periods (Figs. 7a,b, 8a,b,  
241 supplemental animation S3, S4). Similar to the active periods, the tracer field is lofted up over the  
242 land during the day associated with the diurnal heating (Figs. 7a,b, 8a,b, supplemental animation  
243 S3, S4).

244 The tracer field initialized in the marine boundary layer is mostly advected to the north and  
245 exhibits little east–west dispersion for any period (Figs. 9a,b, 10a,b, 11a,b, 12a,b, supplemental  
246 animations S5-8 left panel), consistent with the anticyclonic flow at the surface and within the  
247 boundary layer. Because the tracer field does not penetrate through the top of the boundary layer,  
248 the plan views (Figs. 9a,b, 10a,b, 11a,b, 12a,b, supplemental animations S1-4 left panel; which  
249 show a quasi-integrated quantity of the tracer) can be interpreted as boundary layer thickness (i.e.,  
250 deeper boundary layers mean more tracer in the column and darker shading). This idea can help  
251 to identify any perturbations that move through the boundary layer and cause thickening of the  
252 boundary layer. Animations of these fields show “ripples” — likely internal gravity waves — that  
253 move along the top of the boundary layer in both periods (supplemental animations S5-8). The  
254 right panel of the supplemental animations S5-8 show movies of the cross sections shown in Figs.

255 9c,d, 10c,d, 11c,d, and 12c,d and also show these waves in the boundary layer height (seen both  
256 in the tracer fields themselves and in the calculated boundary layer height). The idea of darker  
257 shading being proportional to a deeper boundary layer also helps to compare the boundary layer  
258 height between the two periods. The plan views of the marine tracer field in the active periods  
259 are lighter than the tracer fields in the null periods, which indicates that the boundary layer in  
260 the null periods is deeper overall than the boundary layer in the active periods (Figs. 9a,b, 10a,b,  
261 11a,b, 12a,b, supplemental animations S5-8 left panel). The deeper boundary layer is additionally  
262 confirmed in the cross sections (Figs. 9c,d, 10c,d, 11c,d, 12c,d, supplemental animations S5-8 right  
263 panel) which show the calculated marine boundary layer height as a dashed line. The differences  
264 in boundary layer height are discussed more in the following sections.

## 265 2) MASS FLUX

266 To better understand the offshore flow in this region, we analyzed the zonal mass flux over the  
267 latitudes annotated by the 200-km wide black line in Figure 1. For each grid column along the  
268 black line, we calculated the profiles of mass flux by multiplying the  $u$  component of the wind by  
269 the air density and then averaged the profiles. Figure 13 shows a time series of these mass flux  
270 profiles over the lowest 2 km for each simulation. Negative values (purple colors) indicate areas  
271 where the flow has an offshore component and positive values (green colors) indicate areas where  
272 the flow has an onshore component. The patterns in each period are consistent with a typical  
273 land-sea breeze circulation with offshore flow overnight (land breeze) and onshore flow during  
274 the day (sea breeze). The areas of overnight offshore flow in the active periods are stronger and  
275 deeper (extending all the way up to 2 km at times) compared to the overnight offshore flow in the  
276 null periods (Fig. 13). Additionally, the null periods typically have stronger onshore flow between  
277 500–1000 m compared to the active periods. The average boundary layer height is visualized by

278 the dashed black line in each image. The overnight offshore flow generally remains above the  
279 boundary layer, with the exception of the second active period where the offshore flow intrudes  
280 into the boundary layer (Fig. 13c).

281 It is possible that the strengthened overnight offshore flow may be explained by cooler temper-  
282 atures over the highlands; however, this is not the case. We calculated the 00 (midnight local  
283 time) UTC temperature averaged over the red box in Figure 1 and compared it to the average mass  
284 flux between 02-05 UTC and 05-08 UTC at 50 m and 100 m above the average boundary layer  
285 height. We found that there is no substantial correlation between the overnight temperature and  
286 the offshore mass flux (Fig. 14).

### 287 *c. Boundary Layer Height*

288 In order to observe the east-west differences in the boundary layer height between the active and  
289 null periods, we calculated the median boundary layer height over 15°S to 20°S and between 0° and  
290 12°E for an overnight period (0200–0600 UTC) for both the active and null periods (Fig. 15). All  
291 periods have a low boundary layer height near the coast (~100–200 m) and then increasing with  
292 height toward the west which is also consistent with the climatological patterns in boundary layer  
293 height for this region. Additionally, the patterns in boundary layer height confirm the idea presented  
294 in the previous sections that the boundary layer height is lower in the active periods than it is in the  
295 null periods. It is important to note that since boundary layer heights are often underestimated in  
296 models (Wyant et al. 2015), the absolute height differences here are not as important as the relative  
297 height differences between the two periods.

## 298 **4. Discussion**

299 Our experimental design simulates active and null periods to determine if there are differences in  
300 mesoscale and synoptic scale conditions which are relevant to potential mechanisms for the cloud-  
301 eroding phenomenon. Our analysis emphasizes the roles of the offshore flow and boundary layer  
302 depth. We ran simulations for the month of May when cloud-eroding boundaries most frequently  
303 occur (Yuter et al. 2018). The underlying reasoning for this choice was that the May average  
304 environment is generally favorable so differences between periods with and without cloud-eroding  
305 boundaries during May would potentially highlight key physical mechanisms.

306 The passive tracer fields and mass flux calculations both indicate that the active periods are  
307 characterized by strong overnight offshore flow and weak afternoon onshore flow. The opposite is  
308 true for the null periods, when the overnight offshore flow is weak and the afternoon onshore flow  
309 is strong. Passive tracers suggest that the offshore flow from the continent during the active period  
310 overrides the marine boundary layer and can extend out as far as 9°E for any given day as compared  
311 to 12°E for null periods. Additionally, the strong afternoon onshore flow in the null periods would  
312 act to suppress both westward advection and gravity-wave propagation. All else being equal, a  
313 shallower boundary layer has thinner stratocumulus clouds than a deeper boundary layer (Wood  
314 2012). Because the active period has a shallower boundary layer than the null period, we infer the  
315 active period clouds are more susceptible to any erosion mechanism compared to the null period.

316 Birch and Reeder (2013) proposed that the interaction of the offshore flow in northwest Australia  
317 with the marine boundary layer triggered gravity waves responsible for wave cloud events in the  
318 region. Since the terrain of the Australian coast slopes downward from about 300 m ASL, terrain  
319 plays only a minimal role in driving a downslope component of the flow. For this reason, the flow  
320 off the continent largely acts as an idealized land-breeze circulation, with the horizontal offshore

321 flow interacting with the marine boundary layer. In contrast to the northwest Australian coast, the  
322 substantial coastal escarpment (maximum altitude 1300 m) along the African coast yields a strong  
323 downslope component of the flow in addition to the land-breeze, which greatly complicates the  
324 interaction between the offshore flow and the marine boundary layer.

325 We propose a conceptual model for interaction between the off-shore flow and marine boundary  
326 layer that includes interactions along both the eastern edge and top edge of the marine boundary  
327 layer (Fig. 16). Even though the downslope flows are driven by nocturnal cooling, adiabatic  
328 warming ensures that the offshore flow remains warmer than the marine boundary layer, leading to  
329 the offshore flow largely overrunning the marine boundary layer. This conceptual model includes  
330 the potential gravity wave trigger of a downward impulse from the offshore flow interacting with  
331 the top of the marine boundary layer. Additionally, the offshore flow moving above the marine  
332 boundary layer would enhance the shear across the boundary layer top, which would promote  
333 enhanced entrainment (i.e. mixing of warm, dry, free-tropospheric air into the boundary layer),  
334 acting to erode the cloud. The details of how the gravity wave and shear would interact remain an  
335 area of future research.

## 336 **5. Conclusions**

337 In this study, we examine the physical mechanisms associated with stratocumulus cloud-eroding  
338 boundaries over the southeast Atlantic. We use the WRF model to run simulations over periods  
339 where several days of cloud-eroding boundaries occur (active periods) and simulations over periods  
340 without cloud-eroding boundaries (null periods). We focus on analyzing the overnight offshore  
341 flow using SLP maps, passive tracer fields, and mass flux calculations. We document different  
342 conditions associated with each period to understand its role in cloud-eroding boundaries. Our  
343 main conclusions are as follows:

- 344 • Active periods with cloud-eroding boundaries have stronger overnight offshore flow than null  
345 periods without clearing events. We propose that the stronger offshore flow likely contributes  
346 to two mechanisms relevant to cloud-eroding boundaries—triggering gravity waves and in-  
347 creasing shear at the top of the marine boundary layer.
  
- 348 • Active periods have lower boundary-layer heights than null periods. A lower marine boundary  
349 layer top is easier for an offshore flow of a given temperature and mass flux to override.  
350 Additionally, lower boundary-layer heights are associated with thinner clouds, which may  
351 cause the clouds in the active period to be more susceptible to erosion.
  
- 352 • The dominant overnight offshore and afternoon onshore flows that delineate active from null  
353 periods are not explained by temperature differences over land. This non-correlation suggests  
354 that there are other factors which contribute to the strength of the offshore flow other than the  
355 cooling over land.

356 Our analysis was not able to separate the temporal and spatial scales between the synoptic  
357 and diurnal. The assumption of a diurnal cycle superimposed over a quasi-steady, barotropic  
358 background is plainly an oversimplification. The background synoptic state is highly varying on  
359 multi-day timescales, as demonstrated by de Szoeke et al. (2016). This reality makes teasing  
360 the two scales apart — and unambiguously identifying the conditions conducive to cloud-eroding  
361 boundaries — highly difficult. As part of disentangling the synoptic and diurnal contributions  
362 to the variability, future analysis should examine the role of the ageostrophic flow during these  
363 periods. Specifically, a more thorough momentum budget analysis should be completed to better  
364 separate the different mechanisms presented in this work.

365 Work by Patricola and Chang (2017) suggests that the shape of the African coastline and resulting  
366 localized convergence and divergence patterns have implications on the coastal jet in this region.

367 Further analysis should examine the associations of the coastal jet as a function of synoptic patterns  
368 in determining days with or without clearing events.

369 A key missing piece to resolving the physical mechanisms responsible for cloud-eroding bound-  
370 aries are the detailed physics occurring within the low cloud deck at convective scales before,  
371 during, and after gravity wave passage. A field experiment centered on the southeast Atlantic  
372 including soundings, lidar, cloud radar, and in situ data sets that transect cloud-eroding boundaries  
373 would advance knowledge and address several key questions.

374 *Data availability statement.* WRF configuration files used to conduct the simulations, and pro-  
375 cessed datasets for some of the figures are available at DOI 10.17605/OSF.IO/X7F5C. The  
376 ERA–Interim product can be downloaded from The NCAR Research Data Archive. For the  
377 full time-dependent 3D WRF simulation output, please contact the corresponding author (Im-  
378 tomkin@ncsu.edu).

379 *Acknowledgments.* The authors greatly appreciate advice and feedback from David Rahn,  
380 Matthew Miller, and Lucas McMichael. This work was supported by NSF AGS grants 1656237  
381 and 1656314 and U.S. Department of Energy grant DE–SC0016522.

## 382 **References**

383 Allen, G., and Coauthors, 2013: Gravity-wave-induced perturbations in marine stratocumulus.  
384 *Quart. J. Roy. Meteor. Soc.*, **139 (670)**, 32–45, doi:10.1002/qj.1952.

385 Birch, C. E., and M. J. Reeder, 2013: Wave-cloud lines over northwest Australia. *Quart. J. Roy.*  
386 *Meteor. Soc.*, **139 (674)**, 1311–1326, doi:10.1002/qj.2043.

- 387 Blaylock, B. K., J. D. Horel, and E. T. Crosman, 2017: Impact of Lake Breezes on Summer  
388 Ozone Concentrations in the Salt Lake Valley. *J. Appl. Meteor. Climatol.*, **56** (2), 353–370,  
389 doi:10.1175/Jamc-D-16-0216.1.
- 390 Bony, S., and J. L. Dufresne, 2005: Marine boundary layer clouds at the heart of tropical cloud feed-  
391 back uncertainties in climate models. *Geophys. Res. Lett.*, **32** (20), doi:10.1029/2005gl023851.
- 392 Connolly, P. J., G. Vaughan, P. Cook, G. Allen, H. Coe, T. W. Choullarton, C. Dearden, and  
393 A. Hill, 2013: Modelling the effects of gravity waves on stratocumulus clouds observed during  
394 VOCALS-UK. *Atmos. Chem. Phys.*, **13** (14), 7133–7152, doi:10.5194/acp-13-7133-2013.
- 395 Crosbie, E., and Coauthors, 2016: Stratocumulus Cloud Clearings and Notable Thermodynamic  
396 and Aerosol Contrasts across the Clear-Cloudy Interface. *Journal of the Atmospheric Sciences*,  
397 **73** (3), 1083–1099, doi:10.1175/Jas-D-15-0137.1.
- 398 de Szoeké, S. P., K. L. Verlinden, S. E. Yuter, and D. B. Mechem, 2016: The Time Scales of  
399 Variability of Marine Low Clouds. *J. Climate*, **29** (18), 6463–6481, doi:10.1175/Jcli-D-15-0460.  
400 1.
- 401 Dee, D. P., and Coauthors, 2011: The ERA-Interim reanalysis: configuration and performance of  
402 the data assimilation system. *Quart. J. Roy. Meteor. Soc.*, **137** (656), 553–597, doi:10.1002/qj.  
403 828.
- 404 Dudhia, J., 1989: Numerical Study of Convection Observed during the Winter Monsoon Experi-  
405 ment Using a Mesoscale Two-Dimensional Model. *Journal of the Atmospheric Sciences*, **46** (20),  
406 3077–3107, doi:10.1175/1520-0469(1989)046<3077:Nsocod>2.0.Co;2.

407 Garreaud, R. D., and R. Muñoz, 2004: The diurnal cycle in circulation and cloudiness over the  
408 subtropical southeast Pacific: A modeling study. *J. Climate*, **17 (8)**, 1699–1710, doi:10.1175/  
409 1520-0442(2004)017<1699:Tdcica>2.0.Co;2.

410 Gelaro, R., and Coauthors, 2017: The Modern-Era Retrospective Analysis for Research and Appli-  
411 cations, Version 2 (MERRA-2). *J. Climate*, **30 (14)**, 5419–5454, doi:10.1175/Jcli-D-16-0758.1.

412 Hartmann, D. L., M. E. Ockertbell, and M. L. Michelsen, 1992: The Effect of Cloud Type on Earths  
413 Energy-Balance - Global Analysis. *J. Climate*, **5 (11)**, 1281–1304, doi:10.1175/1520-0442(1992)  
414 005<1281:Teocto>2.0.Co;2.

415 Hersbach, H., and D. Dee, 2016: ERA-5 reanalysis is in production. *ECMWF newsletter*, 7.

416 Hong, S. Y., Y. Noh, and J. Dudhia, 2006: A new vertical diffusion package with an explicit  
417 treatment of entrainment processes. *Mon. Wea. Rev.*, **134 (9)**, 2318–2341, doi:10.1175/Mwr3199.  
418 1, URL ://WOS:000240654000002.

419 Janjic, Z. I., 1994: The Step-Mountain Eta Coordinate Model - Further Developments of the  
420 Convection, Viscous Sublayer, and Turbulence Closure Schemes. *Mon. Wea. Rev.*, **122 (5)**,  
421 927–945, doi:10.1175/1520-0493(1994)122<0927:Tsmecm>2.0.Co;2.

422 Kain, J. S., 2004: The Kain-Fritsch convective parameterization: An update. *J. Appl. Meteor.*,  
423 **43 (1)**, 170–181, doi:10.1175/1520-0450(2004)043<0170:Tkcpau>2.0.Co;2.

424 Kloesel, K. A., 1992: Marine Stratocumulus Cloud Clearing Episodes Observed during Fire. *Mon.*  
425 *Wea. Rev.*, **120 (4)**, 565–578, doi:10.1175/1520-0493(1992)120<0565:Msceeo>2.0.Co;2.

426 Lin, J.-L., T. Qian, and T. Shinoda, 2014: Stratocumulus clouds in southeastern pacific simulated  
427 by eight cmip5–cfmip global climate models. *JCLI*, **27 (8)**, 3000–3022.

- 428 Mlawer, E. J., S. J. Taubman, P. D. Brown, M. J. Iacono, and S. A. Clough, 1997: Radiative transfer  
429 for inhomogeneous atmospheres: RRTM, a validated correlated-k model for the longwave. *Jour-*  
430 *nal of Geophysical Research-Atmospheres*, **102 (D14)**, 16 663–16 682, doi:10.1029/97jd00237.
- 431 Morrison, H., G. Thompson, and V. Tatarskii, 2009: Impact of Cloud Microphysics on the De-  
432 velopment of Trailing Stratiform Precipitation in a Simulated Squall Line: Comparison of One-  
433 and Two-Moment Schemes. *Mon. Wea. Rev.*, **137 (3)**, 991–1007, doi:10.1175/2008mwr2556.1.
- 434 Nakanishi, M., and H. Niino, 2006: An improved Mellor-Yamada level-3 model: Its numerical  
435 stability and application to a regional prediction of advection fog. *Boundary-Layer Meteorology*,  
436 **119 (2)**, 397–407, doi:10.1007/s10546-005-9030-8.
- 437 Nelson, K. J., D. B. Mechem, and Y. L. Kogan, 2016: Evaluation of Warm-Rain Microphysical  
438 Parameterizations in Mesoscale Simulations of the Cloudy Marine Boundary Layer. *Mon. Wea.*  
439 *Rev.*, **144 (6)**, 2137–2154, doi:10.1175/Mwr-D-15-0266.1.
- 440 O’Dell, C. W., F. J. Wentz, and R. Bennartz, 2008: Cloud liquid water path from satellite-based  
441 passive microwave observations: A new climatology over the global oceans. *J. Climate*, **21 (8)**,  
442 1721–1739, doi:10.1175/2007jcli1958.1.
- 443 Patricola, C. M., and P. Chang, 2017: Structure and dynamics of the benguela low-level coastal  
444 jet. *Climate Dynamics*, **49 (7-8)**, 2765–2788.
- 445 Qian, T., C. C. Epifanio, and F. Zhang, 2012: Topographic effects on the tropical land and sea  
446 breeze. *JAS*, **69 (1)**, 130–149.
- 447 Rahn, D. A., and R. Garreaud, 2010: Marine boundary layer over the subtropical southeast Pacific  
448 during VOCALS-REx - Part 1: Mean structure and diurnal cycle. *Atmos. Chem. Phys.*, **10 (10)**,  
449 4491–4506, doi:10.5194/acp-10-4491-2010.

- 450 Skamarock, W. C., and Coauthors, 2008: A Description of the Advanced Research WRF Version  
451 3. *NCAR Tech. Note NCAR/TN-475+STR*, 113, doi:10.5065/D68S4MVH.
- 452 Smagorinsky, J., 1963: General circulation experiments with the primitive equations: I. The basic  
453 experiment. *Mon. Wea. Rev.*, **91** (3), 99–164.
- 454 Tewari, M., and Coauthors, 2004: Implementation and verification of the unified NOAA land  
455 surface model in the WRF model. *20th conf. on weather analysis and forecasting/16th conf. on  
456 numerical weather prediction*, Vol. 1115, 2165–2170.
- 457 Wood, R., 2012: Stratocumulus Clouds. *Mon. Wea. Rev.*, **140** (8), 2373–2423, doi:10.1175/  
458 Mwr-D-11-00121.1.
- 459 Wyant, M. C., and Coauthors, 2015: Global and regional modeling of clouds and aerosols in  
460 the marine boundary layer during VOCALS: the VOCA intercomparison. *Atmos. Chem. Phys.*,  
461 **15** (1), 153–172, doi:10.5194/acp-15-153-2015.
- 462 Yuter, S. E., J. D. Hader, M. A. Miller, and D. B. Mechem, 2018: Abrupt cloud clearing of marine  
463 stratocumulus in the subtropical southeast Atlantic. *Science*, doi:10.1126/science.aar5836.
- 464 Zuidema, P., and Coauthors, 2016: Challenges and Prospects for Reducing Coupled Climate  
465 Model SST Biases in the Eastern Tropical Atlantic and Pacific Oceans: The U.S. CLIVAR  
466 Eastern Tropical Oceans Synthesis Working Group. *Bull. Amer. Meteor. Soc.*, **97** (12), 2305–+,  
467 doi:10.1175/Bams-D-15-00274.1.

468 **LIST OF TABLES**

469 **Table 1.** Dates and clearing event characteristic (“yes”, “no”, “maybe”; see text for full  
470 description) of each simulation. Italicized dates indicate those not analyzed to  
471 account for spin-up. . . . . 24

472 TABLE 1. Dates and clearing event characteristic (“yes”, “no”, “maybe”; see text for full description) of each  
 473 simulation. Italicized dates indicate those not analyzed to account for spin-up.

Active #1		Active #2		Null #1		Null #2	
<i>20 May 2013</i>	YES	<i>22 May 2014</i>	NO	<i>21 May 2008</i>	NO	<i>01 May 2009</i>	NO
21 May 2013	NO	23 May 2014	YES	22 May 2008	NO	02 May 2009	NO
22 May 2013	YES	24 May 2014	YES	23 May 2008	NO	03 May 2009	NO
23 May 2013	NO	25 May 2014	YES	24 May 2008	NO	04 May 2009	NO
24 May 2013	YES	26 May 2014	YES	25 May 2008	NO	05 May 2009	NO
25 May 2013	YES	27 May 2014	YES	26 May 2008	NO	06 May 2009	NO
26 May 2013	YES	28 May 2014	YES	27 May 2008	NO	07 May 2009	NO

474 **LIST OF FIGURES**

475 **Fig. 1.** WRF domain configuration for the simulations with terrain (m; contoured every 50 m). Mesh  
476 D01 (black box) has horizontal grid spacing of 10 km. Fine mesh simulations with grid  
477 spacing 3.33 km have been performed but are not included in this report or on this figure.  
478 Red box indicates location of temperature analysis, black line indicates locations of mass  
479 flux calculations completed later in the analysis. . . . . 27

480 **Fig. 2.** Vertical grid spacing in the model as a function of height for (a) lower 5 km and (b) full  
481 model vertical extent. Red box in (b) shows location of (a). . . . . 28

482 **Fig. 3.** 2-m temperatures diurnal cycle for WRF (bold black line), ERA–Interim (red line), ERA5  
483 (blue line), and MERRA2 (green line) data valid for 20 May 2013 0000 UTC to 27 May  
484 2013 0000 UTC averaged over 15–20°S, 15–20°E. . . . . 29

485 **Fig. 4.** Simulated sea-level pressure (hPa; contoured every 1 hPa) and 10-m winds (key in upper  
486 right) for a representative time in the middle of the (a) Active # 1 (24 May 2013 00 UTC),  
487 (b) Null # 1 (25 May 2008 00 UTC), (c) Active #2 (26 May 2014 00 UTC), and (d) Null # 2  
488 (5 May 2009 00 UTC) simulations. . . . . 30

489 **Fig. 5.** (a)–(b) Plan views of the simulated column-integrated ‘land’ passive tracer field (red shaded,  
490 dimensionless) for two times during the active # 1 period (24 May 2013 0000 UTC and 27  
491 May 2013 0000 UTC). (c)–(d) Vertical cross section of tracer along 15.5°S line indicated in  
492 (a) and (b) and boundary layer height (dashed black line). . . . . 31

493 **Fig. 6.** As in Fig. 5 but for two times during the active #2 period (26 May 2014 0000 UTC and 29  
494 May 2014 0000 UTC). . . . . 32

495 **Fig. 7.** As in Fig. 5 but for two times during the null #1 period (25 May 2008 0000 UTC and 28  
496 May 2008 0000 UTC). . . . . 33

497 **Fig. 8.** As in Fig. 5 but for two times during the null #2 period (5 May 2009 0000 UTC and 8 May  
498 2009 0000 UTC). . . . . 34

499 **Fig. 9.** (a)–(b) Plan views of the simulated column-integrated ‘ocean’ passive tracer field (blue  
500 shaded, dimensionless) for the same two active # 1 period times as in Fig. 5. (c)–(d) Vertical  
501 cross section of tracer along 15.5°S line indicated in (a) and (b) and boundary layer height  
502 (dashed black line). . . . . 35

503 **Fig. 10.** As in Fig. 9 but for the same two active #2 period times as in Fig. 6. . . . . 36

504 **Fig. 11.** As in Fig. 9 but for the same two null #1 period times as in Fig. 7. . . . . 37

505 **Fig. 12.** As in Fig. 9 but for the same two null #2 period times as in Fig. 8. . . . . 38

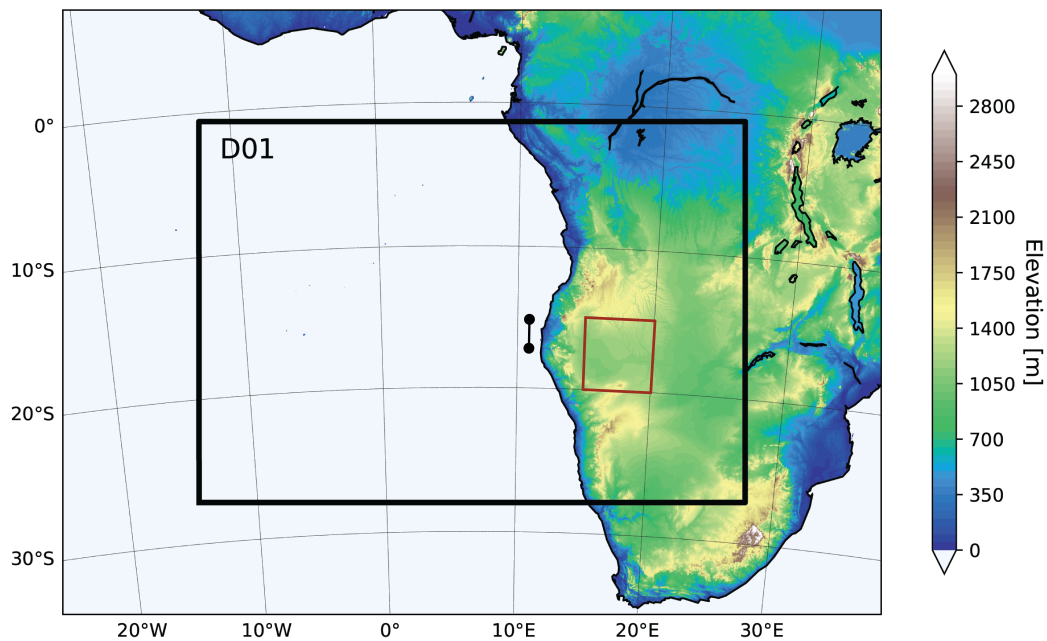
506 **Fig. 13.** Time series of mass flux ( $kgm^{-2}s^{-1}$ ) from 0 m to 2000 m every 50 m for (a) Active # 1  
507 period, (b) Null # 1 period, (c) Active #2 period, and (d) Null #2 period. Dashed black line  
508 shows averaged boundary layer height. Purple colors indicate areas where there is offshore  
509 flow and green colors indicate areas where there is onshore flow. . . . . 39

510 **Fig. 14.** Scatter plot of 00 UTC temperature averaged over red box in Figure 1 compared to 02-05  
511 UTC (left) and 05-08 UTC (left) average mass flux from black line in Figure 1. Points are  
512 distinguished for each simulation, Active #1 (dark blue), Active #2 (light blue), Null #1 (dark

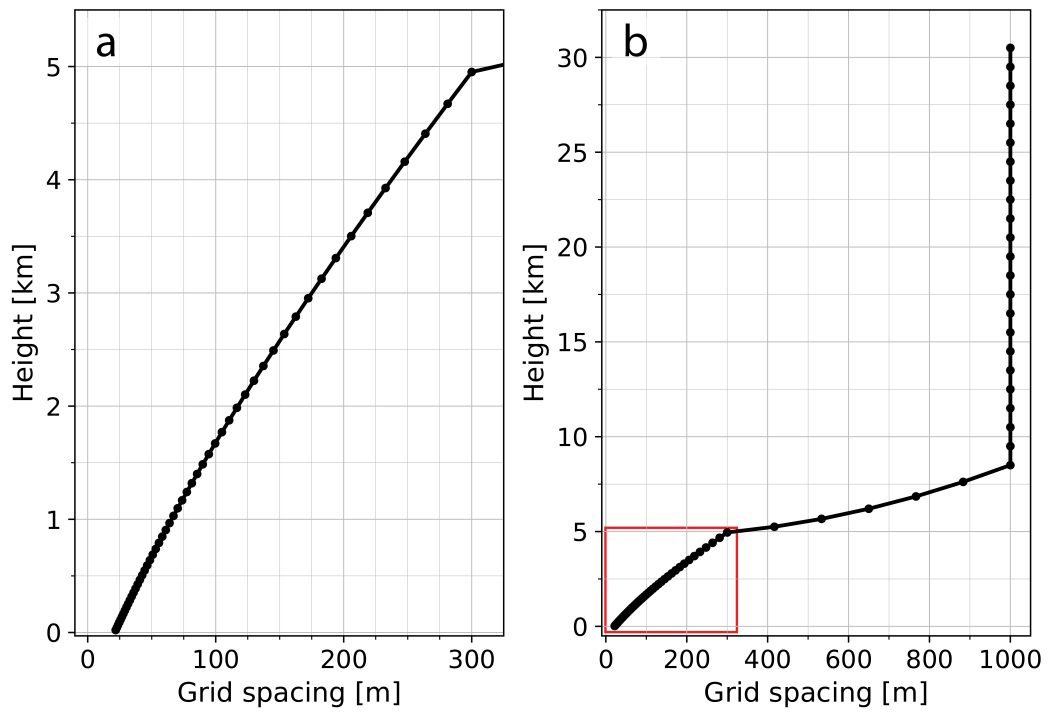
513 green), and Null #2 (light green) and for 50 m (circles) and 100 m (squares) above the average  
514 boundary layer height. . . . . 40

515 **Fig. 15.** Calculated median boundary layer height (m) as a function of longitude calculated over a  
516 latitude range from 15°S to 20°S for the Active #1 period (dark blue), Active #2 period  
517 (light blue), Null #1 period (dark green) and Null #2 period (light green) during the night  
518 (0200–0600 UTC). Shaded regions show the interquartile range. . . . . 41

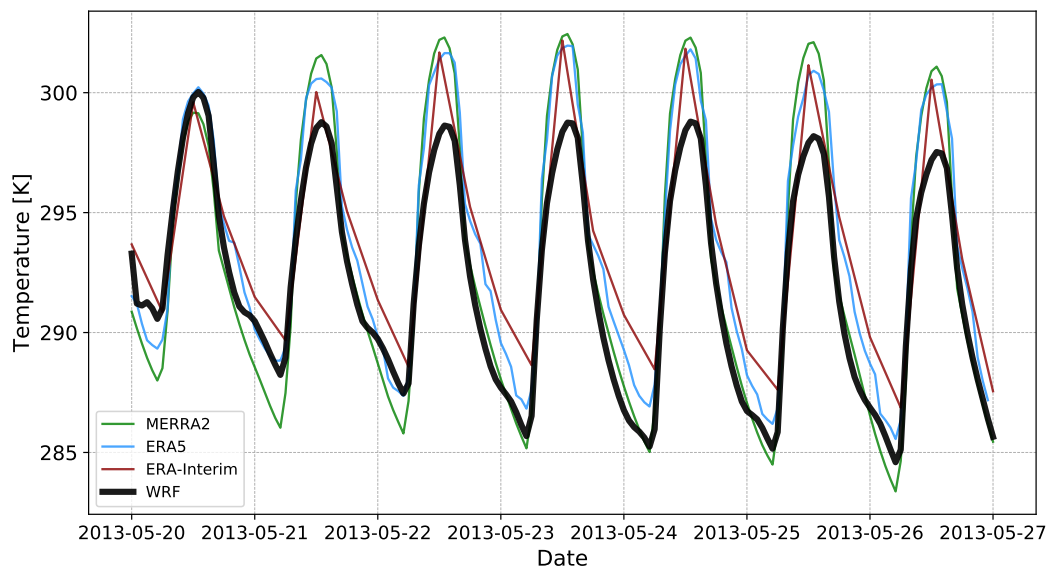
519 **Fig. 16.** Conceptual model showing cross sections for 3 sequential times (a–c) during a cloud-eroding  
520 event. The cross sections are along a representative latitude (e.g. 15.5°S as in Figs. 5–12)  
521 and indicate the relative locations of the MBL top (black line) and land (brown). Gray  
522 arrows represent the offshore flow from the continent. Blue dashed line at 12°E in (b) and (c)  
523 indicate the original position of the MBL edge in (a). The red arrow in (b) shows the motion  
524 of the gravity wave. The green box in (c) indicates a region of shear instability generated by  
525 the offshore flow overriding the MBL. . . . . 42



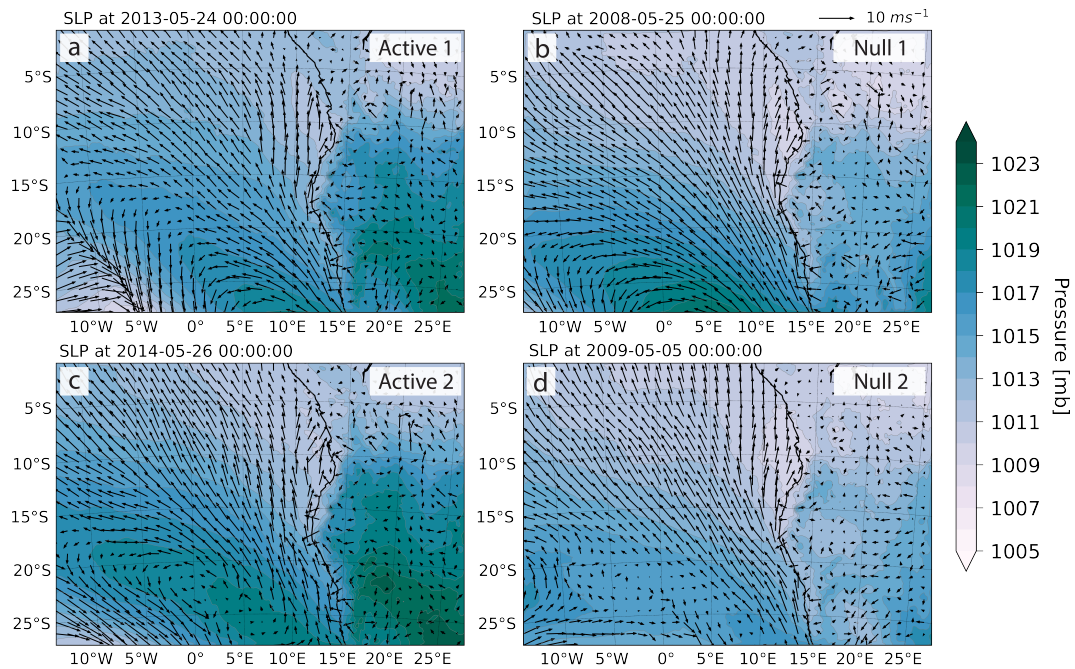
526 FIG. 1. WRF domain configuration for the simulations with terrain (m; contoured every 50 m). Mesh D01  
 527 (black box) has horizontal grid spacing of 10 km. Fine mesh simulations with grid spacing 3.33 km have been  
 528 performed but are not included in this report or on this figure. Red box indicates location of temperature analysis,  
 529 black line indicates locations of mass flux calculations completed later in the analysis.



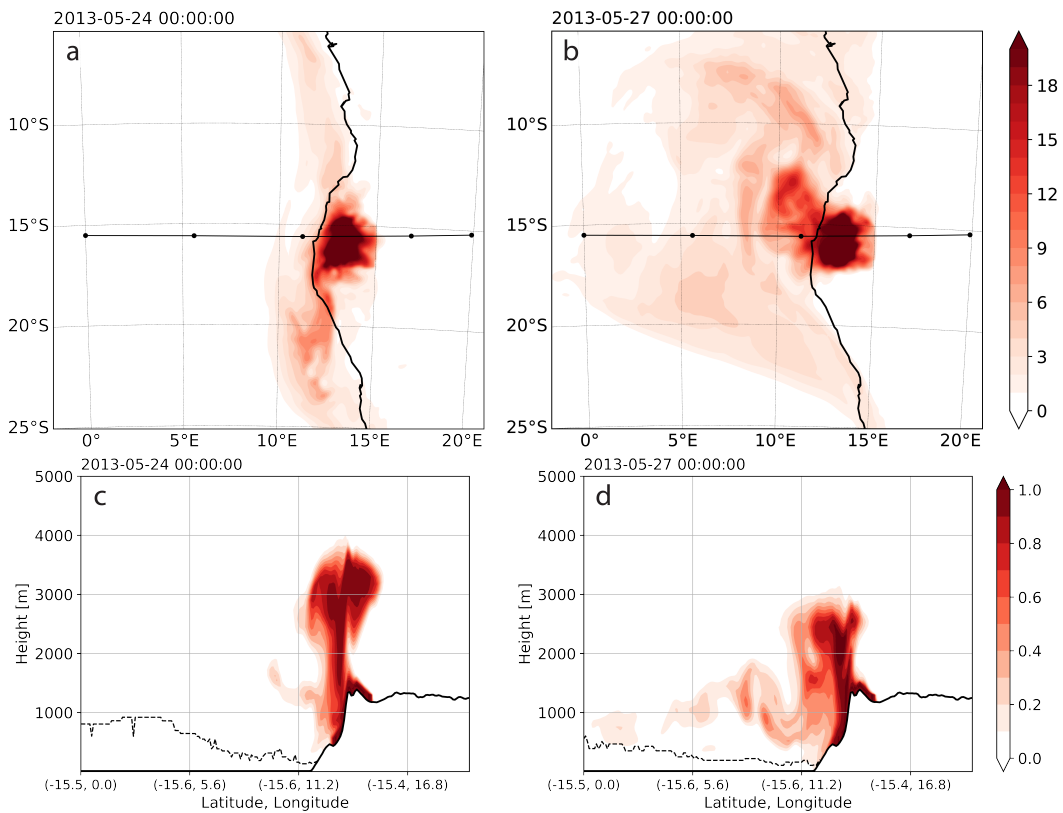
530 FIG. 2. Vertical grid spacing in the model as a function of height for (a) lower 5 km and (b) full model vertical  
 531 extent. Red box in (b) shows location of (a).



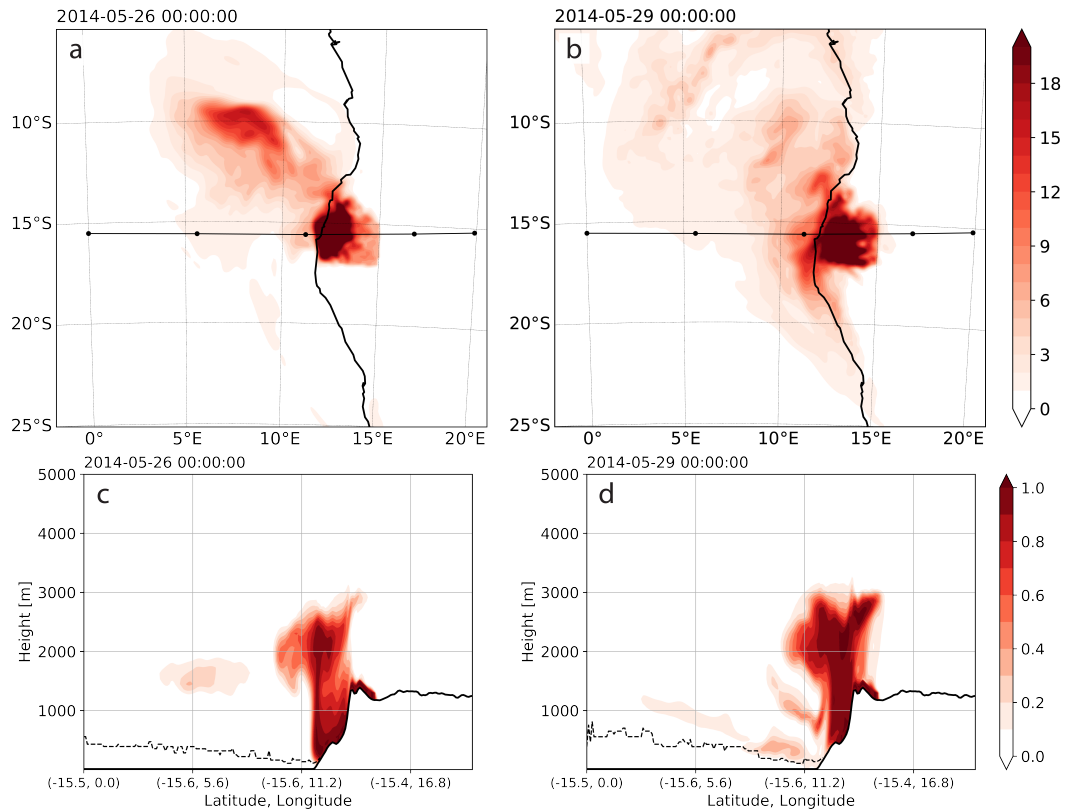
532 FIG. 3. 2-m temperatures diurnal cycle for WRF (bold black line), ERA-Interim (red line), ERA5 (blue line),  
 533 and MERRA2 (green line) data valid for 20 May 2013 0000 UTC to 27 May 2013 0000 UTC averaged over  
 534 15–20°S, 15–20°E.



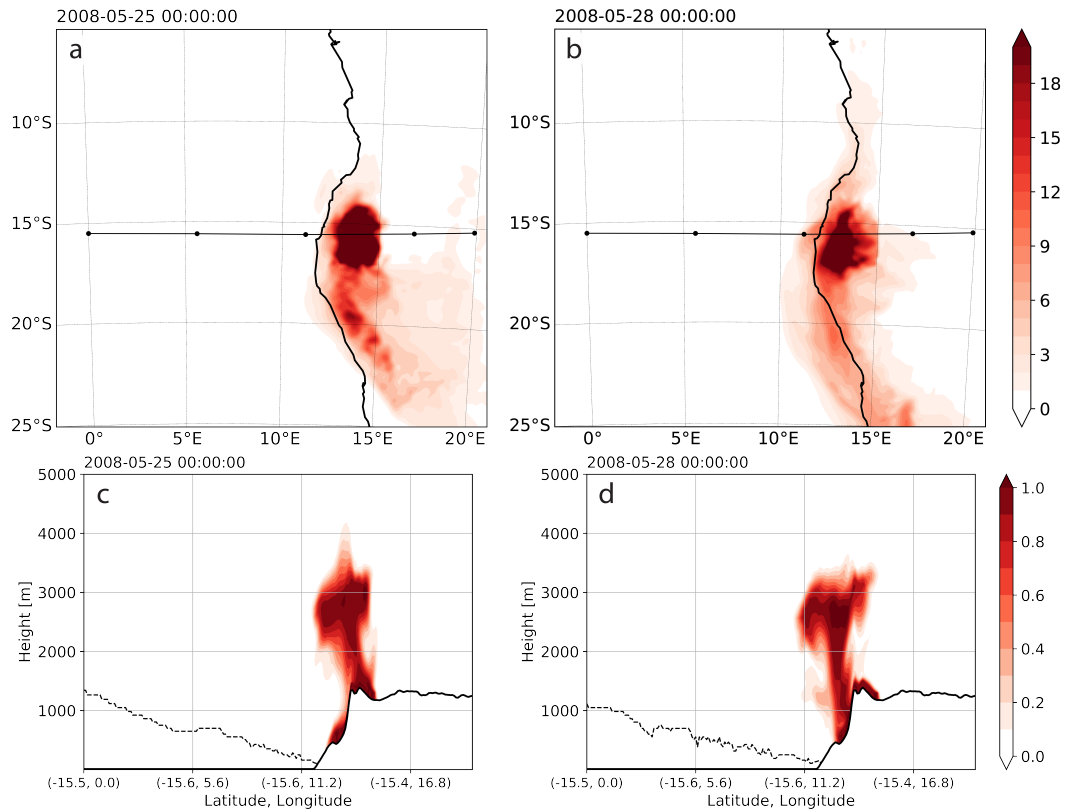
535 FIG. 4. Simulated sea-level pressure (hPa; contoured every 1 hPa) and 10-m winds (key in upper right) for a  
 536 representative time in the middle of the (a) Active # 1 (24 May 2013 00 UTC), (b) Null # 1 (25 May 2008 00  
 537 UTC), (c) Active #2 (26 May 2014 00 UTC), and (d) Null # 2 (5 May 2009 00 UTC) simulations.



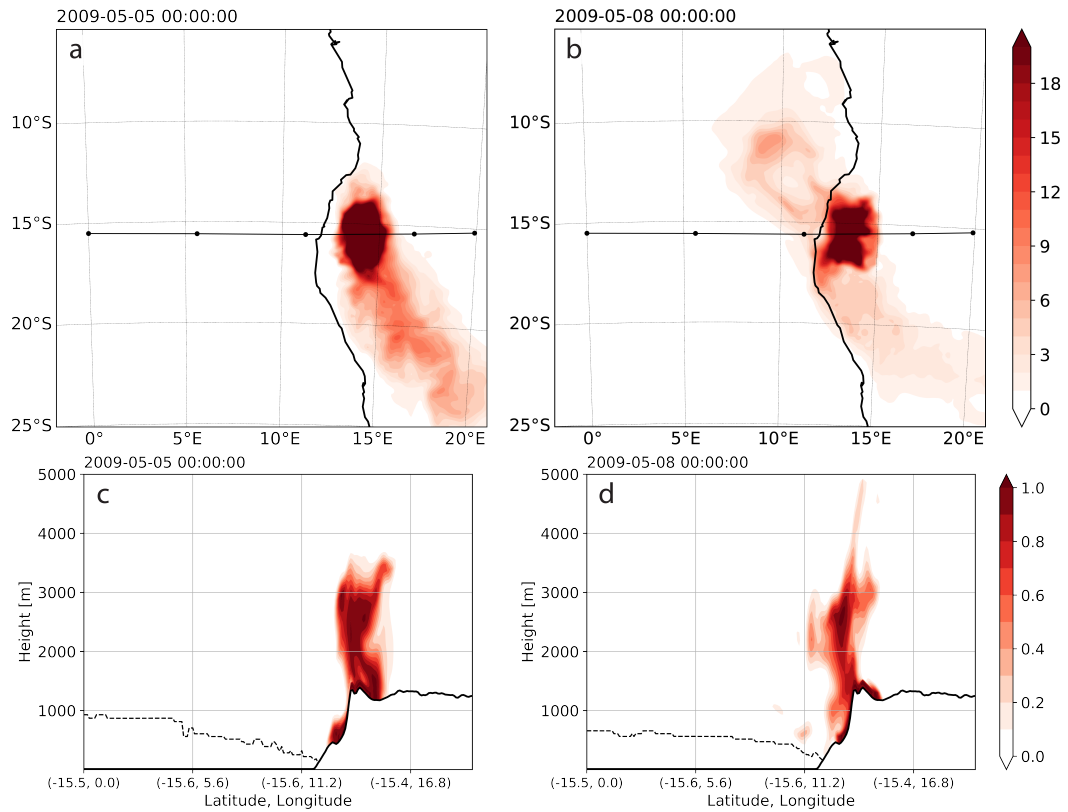
538 FIG. 5. (a)–(b) Plan views of the simulated column-integrated ‘land’ passive tracer field (red shaded, dimen-  
 539 sionless) for two times during the active # 1 period (24 May 2013 0000 UTC and 27 May 2013 0000 UTC).  
 540 (c)–(d) Vertical cross section of tracer along 15.5°S line indicated in (a) and (b) and boundary layer height  
 541 (dashed black line).



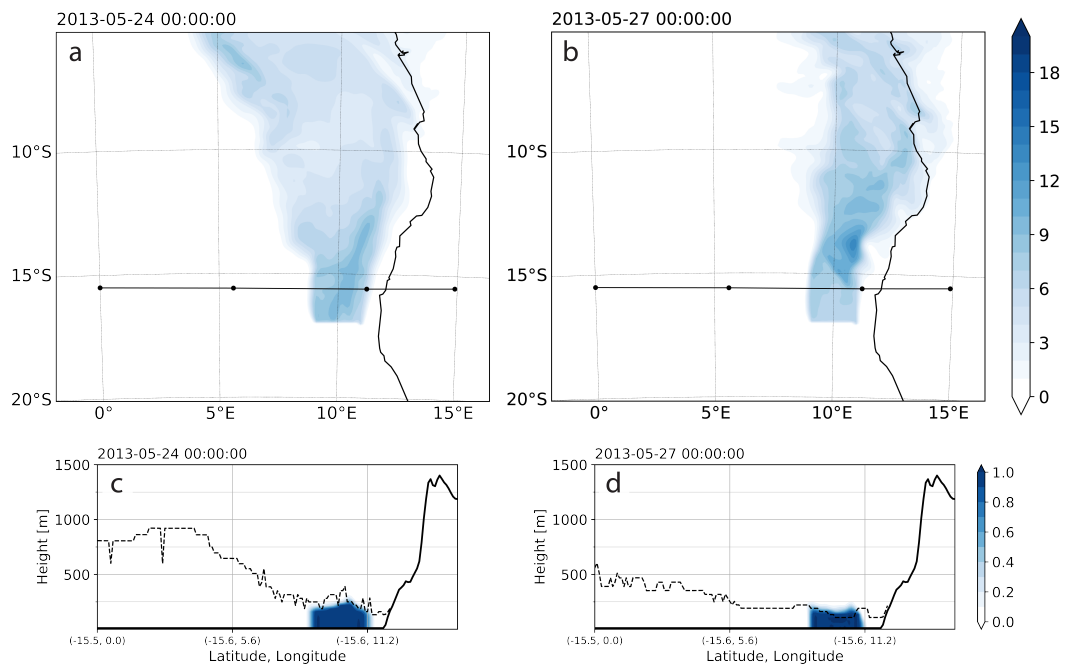
542 FIG. 6. As in Fig. 5 but for two times during the active #2 period (26 May 2014 0000 UTC and 29 May 2014  
 543 0000 UTC).



544 FIG. 7. As in Fig. 5 but for two times during the null #1 period (25 May 2008 0000 UTC and 28 May 2008  
 545 0000 UTC).



546 FIG. 8. As in Fig. 5 but for two times during the null #2 period (5 May 2009 0000 UTC and 8 May 2009 0000  
 547 UTC).



548 FIG. 9. (a)–(b) Plan views of the simulated column-integrated ‘ocean’ passive tracer field (blue shaded,  
 549 dimensionless) for the same two active # 1 period times as in Fig. 5. (c)–(d) Vertical cross section of tracer along  
 550 15.5°S line indicated in (a) and (b) and boundary layer height (dashed black line).

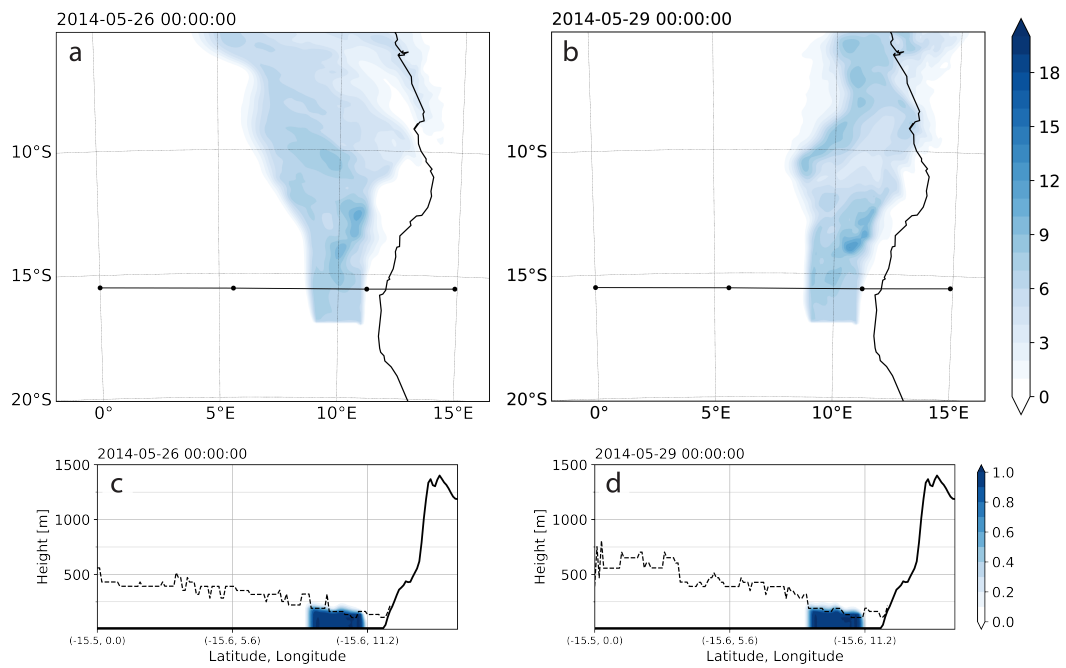


FIG. 10. As in Fig. 9 but for the same two active #2 period times as in Fig. 6.

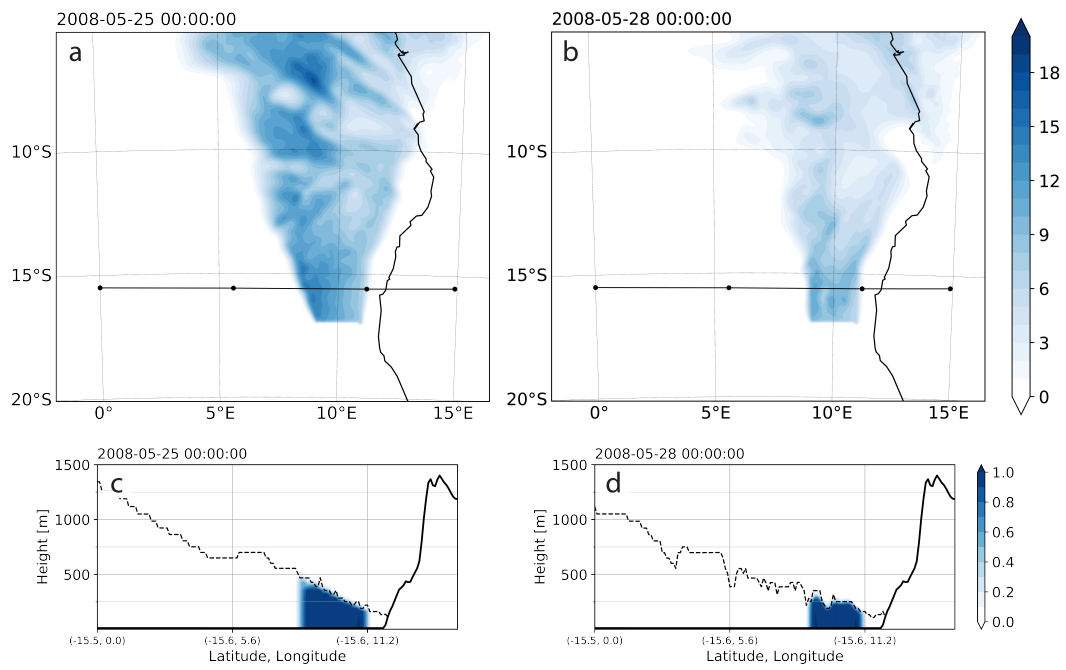


FIG. 11. As in Fig. 9 but for the same two null #1 period times as in Fig. 7.

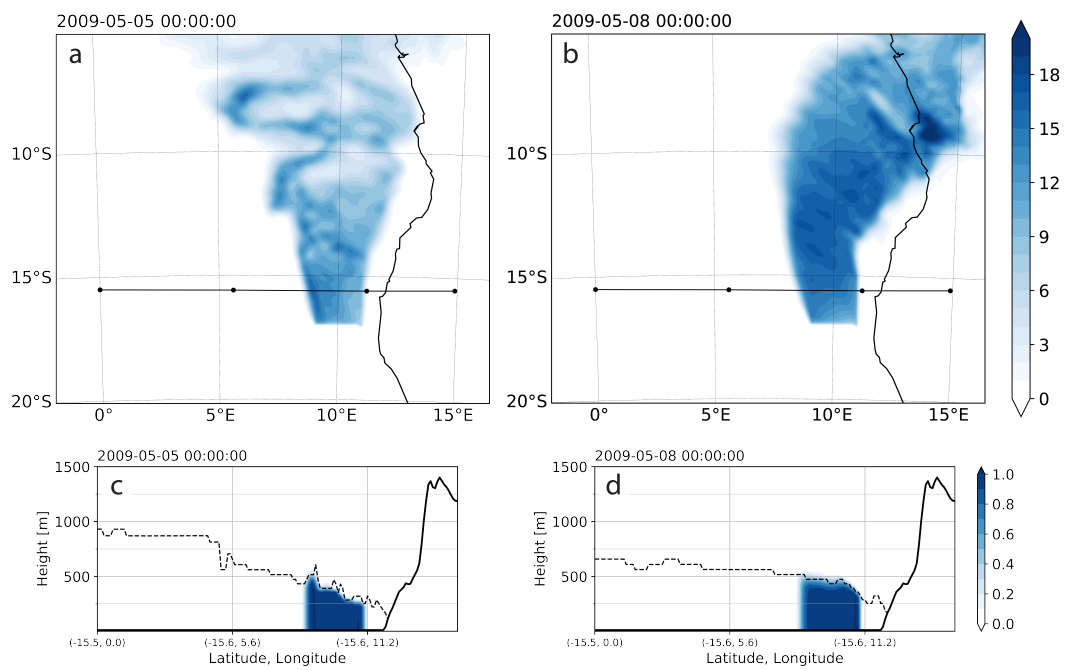
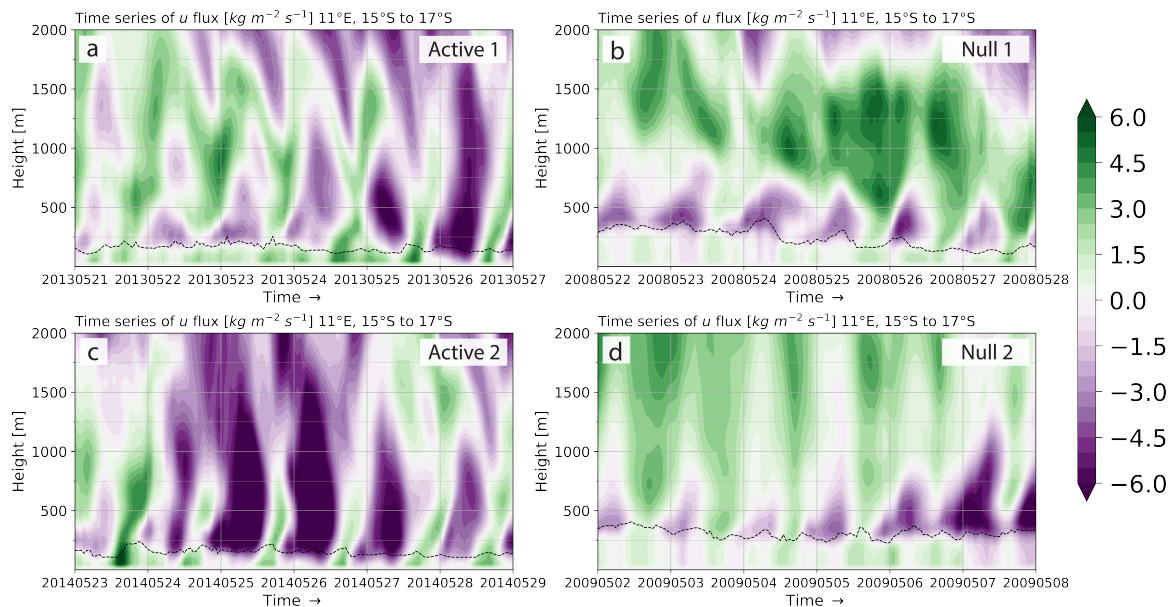
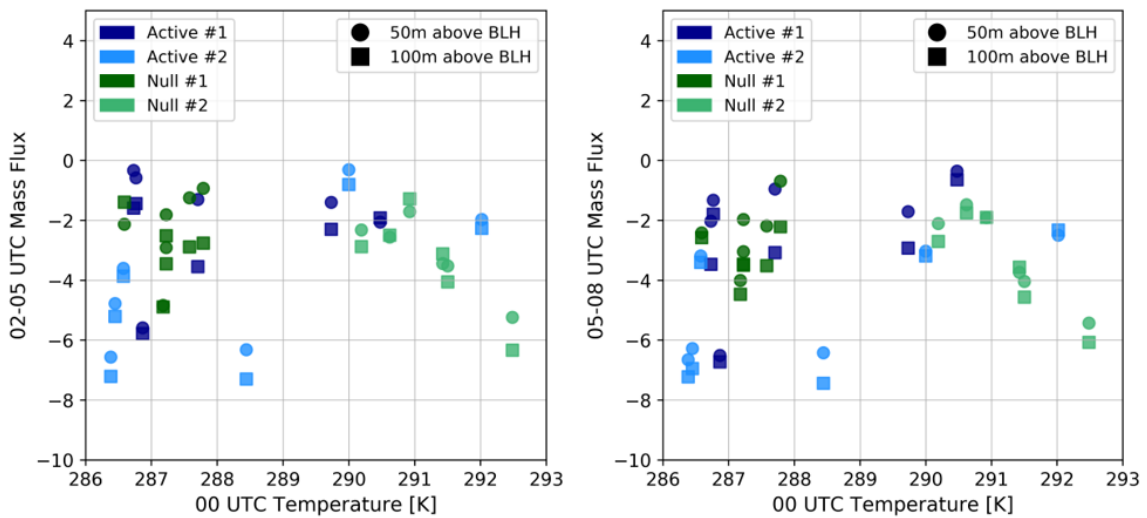


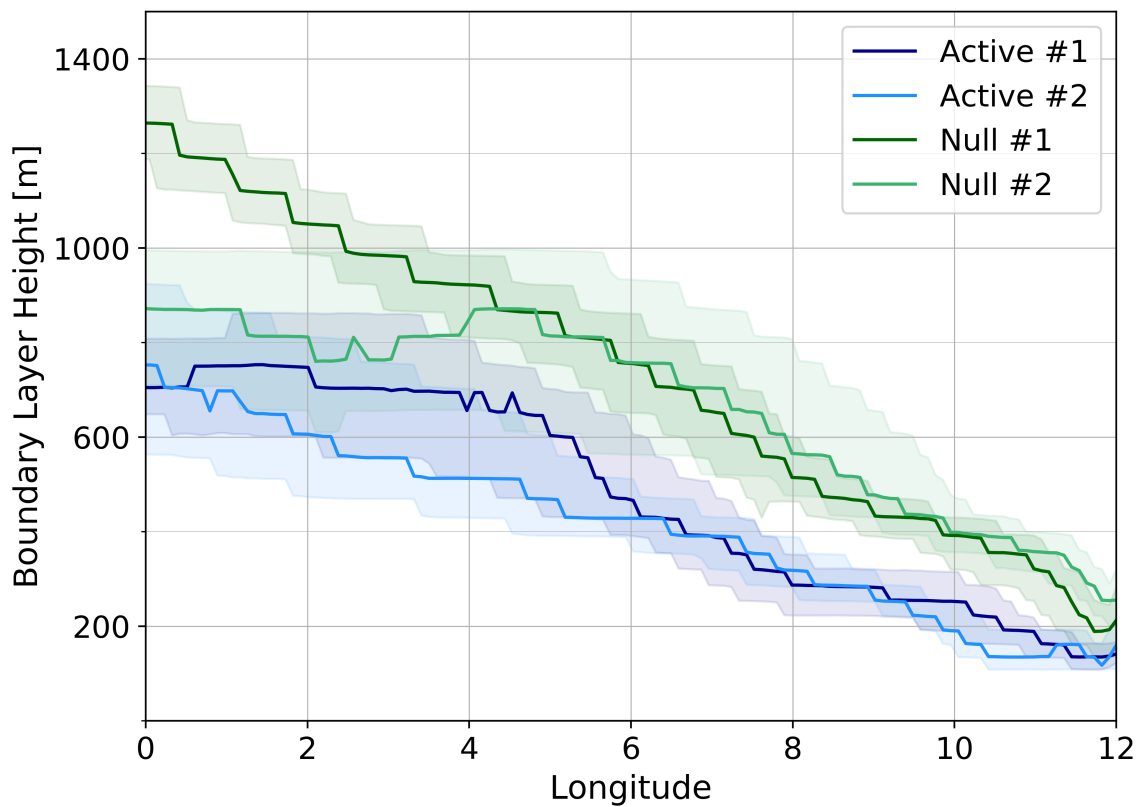
FIG. 12. As in Fig. 9 but for the same two null #2 period times as in Fig. 8.



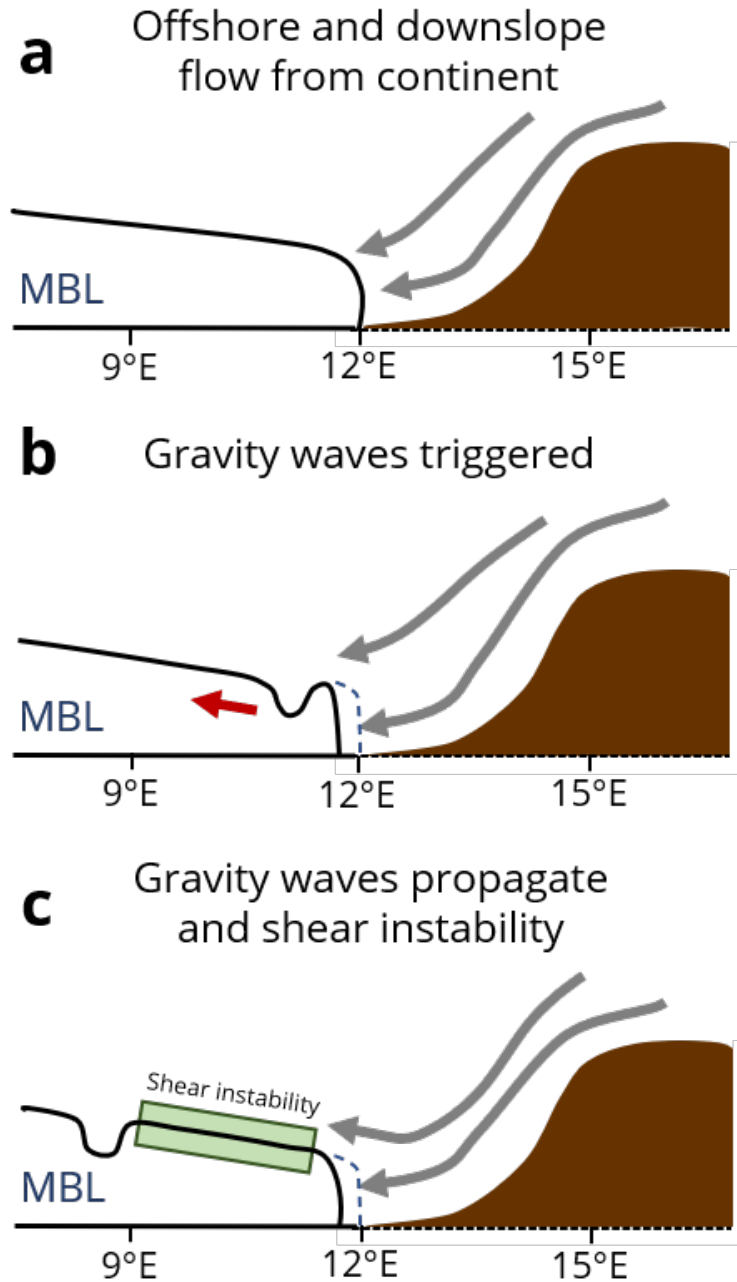
551 FIG. 13. Time series of mass flux ( $kg\ m^{-2}\ s^{-1}$ ) from 0 m to 2000 m every 50 m for (a) Active # 1 period, (b)  
 552 Null # 1 period, (c) Active #2 period, and (d) Null #2 period. Dashed black line shows averaged boundary layer  
 553 height. Purple colors indicate areas where there is offshore flow and green colors indicate areas where there is  
 554 onshore flow.



555 FIG. 14. Scatter plot of 00 UTC temperature averaged over red box in Figure 1 compared to 02-05 UTC (left)  
 556 and 05-08 UTC (left) average mass flux from black line in Figure 1. Points are distinguished for each simulation,  
 557 Active #1 (dark blue), Active #2 (light blue), Null #1 (dark green), and Null #2 (light green) and for 50 m (circles)  
 558 and 100 m (squares) above the average boundary layer height.



559 FIG. 15. Calculated median boundary layer height (m) as a function of longitude calculated over a latitude  
 560 range from 15°S to 20°S for the Active #1 period (dark blue), Active #2 period (light blue), Null #1 period (dark  
 561 green) and Null #2 period (light green) during the night (0200–0600 UTC). Shaded regions show the interquartile  
 562 range.



563 FIG. 16. Conceptual model showing cross sections for 3 sequential times (a–c) during a cloud-eroding event.  
 564 The cross sections are along a representative latitude (e.g. 15.5°S as in Figs. 5–12) and indicate the relative  
 565 locations of the MBL top (black line) and land (brown). Gray arrows represent the offshore flow from the  
 566 continent. Blue dashed line at 12°E in (b) and (c) indicate the original position of the MBL edge in (a). The red  
 567 arrow in (b) shows the motion of the gravity wave. The green box in (c) indicates a region of shear instability  
 568 generated by the offshore flow overriding the MBL.